Epitaxial Ferrimagnetic Mn_4N Thin Films on GaN by Molecular Beam Epitaxy

Zexuan Zhang[1], Yongjin Cho[1], Mingli Gong[2], Shao-Ting Ho[2], Jashan Singhal[1], Jimy Encomendero[1], Xiang Li[1], Hyunjea Lee[1], Huili Grace Xing[1,2,3], and Debdeep Jena[1,2,3]

[1]School of Electrical and Computer Engineering, Cornell University, Ithaca, NY 14853 USA
[2]Department of Materials Science and Engineering, Cornell University, Ithaca, NY 14853 USA
[3]Kavli Institute at Cornell for Nanoscale Science, Ithaca, NY 14853 USA

Direct epitaxial integration of magnetic layers with wide bandgap nitride semiconductors will enable spin-controlled transport and photonic phenomena, seeding ideas for functional spintronic devices. Using plasma-assisted molecular beam epitaxy (MBE) in a previously unexplored window, significantly improved ferrimagnetic Mn_4N layers are successfully grown on GaN with ∼1 nm surface roughness. Distinct from earlier reports, the Mn_4N layers grown on GaN are found to be [001] oriented with 12-fold in-plane symmetry in the diffraction pattern. This unique epitaxial registry originates from three equivalent rotational domains. The ferrimagnetic magnetotransport properties of low growth temperature Mn_4N layers on GaN are comparable to those reported on cubic substrates such as MgO. However, a sign-flip of the Hall resistance is discovered for Mn_4N layers grown above 300 °C.

***Index Terms*— Ferrimagnet, gallium nitride, Hall effect, manganese nitride, molecular beam epitaxy (MBE), wide bandgap semiconductor.**

I. Introduction

THE III-nitride family of wide bandgap semiconductors GaN, AlN, and their alloys are important for diverse applications ranging from solid-state lighting to RF and power electronics [1], [2]. Intrinsically weak spin–orbit coupling in this wide bandgap semiconductor family [3], [4] results in long spin lifetimes and spin mean-free paths [5]. The nitride semiconductor platform is therefore attractive for exploiting the spin degree of freedom of conducting electrons. The ferromagnet/semiconductor heterostructure is crucial for fundamental spin-related device building blocks such as spin injection, spin transport, spin detection [3], [4], [6]–[9], and spin to charge conversion [10]–[12]. Proof-of-concept devices such as spin LEDs [13]–[16] and spintronic terahertz generation [17] relying on the ferromagnet/semiconductor heterostructure have been explored in the nitride semiconductor platform.

Magnetic tunnel junctions and memory devices utilizing spin–orbit torques require smooth interfaces between ferromagnets and the heavy metal or topological insulator layers on top for efficient spin transmission [18], [19]. Therefore, epitaxial growth of magnetic layers with *smooth* surfaces on GaN hosting desirable properties for spintronic applications will provide a path toward spintronic devices for energy-efficient memory applications, and its integration with GaN-based RF, photonic, and wide bandgap CMOS platforms [20], [21]. Such integration is desirable to lower the existing barriers between logic, memory, and communication functionalities, the three pillars of electronic information systems [2].

Mn_4N, a metallic nitride ferrimagnet, is an attractive candidate for direct epitaxial integration with GaN and AlN for all-nitride ferromagnet/semiconductor heterostructures. Molecular beam epitaxy (MBE) grown Mn_4N thin films on cubic substrates such as MgO and $SrTiO_3$ (STO) exhibit desirable properties for spintronic applications such as a high critical temperature ($T_N \sim 740$ K) [22], [23], large spin polarization ($P \sim 70$ %) [22], [24], strong perpendicular magnetic anisotropy ($K_u = 1.1 \times 10^5$ J/m^3) [22], [25]–[31], low saturation magnetization ($M_s = 7.1 \times 10^4$ A/m on STO) [22], [28], large domains (∼ millimeter size on STO) [28], and high domain wall velocities (up to 900 m/s) [22]. Furthermore, the magnetic properties of Mn_4N are tunable toward the magnetic compensation point by alloying with other transition metal elements such as Co [32], [33] and Ni [34], [35]. Epitaxial growth of single crystalline Mn_4N on the wide bandgap semiconductor SiC with smooth surface has been reported using reactive MBE with a NH_3 source for nitrogen [36]. Though the authors mentioned Mn_4N on GaN in that report, they presented no data. In our recent report [27], Mn_4N layers grown on GaN using plasma-assisted MBE at similar growth temperatures as in [36] were found to be polycrystalline with rough surfaces. A systematic study of the influence of growth conditions on the surface smoothness, and structural and magnetic properties of Mn_4N grown on GaN, is lacking.

In this article, we uncover plasma-assisted MBE growth conditions needed for significantly improved epitaxial growth of *c*-axis aligned Mn_4N on GaN with smooth surface morphologies, with root mean square (rms) roughness ∼1 nm. This is achieved by exploration of nucleation and growth conditions. The optimal growth window and the epitaxial relationship for plasma-MBE are found to be remarkably different from the earlier report using reactive MBE [36]. Instead of out-of-plane [111] orientation of Mn_4N on GaN as found in reactive MBE [36], Mn_4N layers grown using plasma-assisted MBE in this work are dominated by [001] orientation with 12-fold in-plane symmetry in the diffraction pattern. Smooth Mn_4N layers are obtained at low growth

Manuscript received March 16, 2021; revised May 12, 2021; accepted May 25, 2021. Date of publication June 4, 2021; date of current version January 20, 2022. Corresponding author: Z. Zhang (e-mail: zz523@cornell.edu).
Color versions of one or more figures in this article are available at https://doi.org/10.1109/TMAG.2021.3085853.
Digital Object Identifier 10.1109/TMAG.2021.3085853

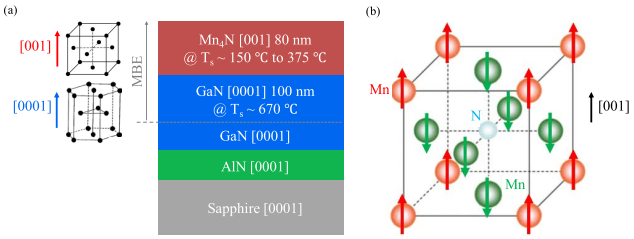

Fig. 1. (a) Schematic of the epitaxial structures in this study. (b) Crystal and magnetic structure of Mn_4N.

temperatures of $T_s \leq 300$ °C. The anomalous Hall resistance hysteresis loops are less square for low-temperature growths compared to those grown at high temperatures. Interestingly, a flip in the anomalous Hall resistance sign is discovered: n-type like behavior is seen for $T_s \leq 225$ °C, and p-type like behavior for $T_s \geq 300$ °C. We first discuss the growth and characterization methods in Section II, and the results in Section III, and conclude in Section IV.

II. Growth and Characterization Methods

The epitaxial structures in this study were grown in a Veeco GENXplor MBE system. High purity elemental Ga and Mn effusion cells supplied the metal fluxes, and ultra-high purity nitrogen gas was supplied through a plasma source. KSA Instruments reflection high-energy electron diffraction (RHEED) apparatus with a Staib electron gun operating at 14.5 kV and 1.45 A was used to *in situ* monitor the surface crystal structure during film growth.

Semi-insulating GaN/sapphire templates from PAM-Xiamen were ultrasonicated for 20 min in acetone, methanol, and isopropanol successively and glued with indium on silicon carrier wafers. Before introducing into the growth module, the substrates were baked at 200 °C overnight for 8 h in a ultra-high vacuum (UHV) preparation chamber.

Fig. 1(a) shows the layer structures investigated. Before the deposition of Mn_4N layers, 100 nm homoepitaxial undoped GaN buffer layers were first grown at a thermocouple temperature of 670 °C. A Ga beam equivalent pressure (BEP) of 1×10^{-6} Torr and nitrogen plasma operating at 200 W with N_2 gas flow rate of 1.95 sccm was used. Excess Ga droplets were *in situ* desorbed at the GaN growth temperature. This was monitored by RHEED intensity change; some Ga-droplet remnants are not ruled out. The substrate was then cooled down to the desired Mn_4N growth temperatures for various samples. 80 nm Mn_4N layers were subsequently deposited with a Mn BEP of 4×10^{-7} Torr and nitrogen plasma operating at 80 W with an N_2 gas flow rate of 0.45 sccm. The schematic of the epitaxial structure in this study is shown in Fig. 1(a). A series of four samples were grown in which the growth temperature of the Mn_4N layer was varied from $T_s = 150$ °C to $T_s = 375$ °C. A control sample of Mn_4N on MgO was grown for comparative studies.

After growth, the crystalline phase and crystal orientation of the films were characterized using XRD with a Panalytical XPert Pro setup at 45 kV and 40 mA with the Cu Kα1 radiation ($\lambda = 1.5406$ Å). The surface morphology of the material stack was measured using atomic force microscopy (AFM) in an Asylum Research Cipher ES setup. A Lakeshore Hall-effect system with a 1 T electromagnet was used for magnetotransport measurements on blanket layers in Van der Pauw geometry. Magnetization of the films was characterized using a Quantum Design Physical Property Measurement System (PPMS) with magnetic fields up to 9 T. All the magnetic property measurements in this study were performed at 300 K unless otherwise noted.

III. Results and Discussion

Fig. 1(b) shows the anti-perovskite crystal structure of Mn_4N, belonging to the space group $P4\bar{3}m$. Mn atoms at the corners (red color) have a magnetic moment of $3.85\mu_B$ pointing along one direction and those at the face centers (green color) have $0.9\mu_B$ pointing in the opposite direction [37]. Here, $\mu_B = (e\hbar/2m_e)$ is the elementary Bohr magneton, where e is the electron charge, m_e is the electron rest mass, and $\hbar = (h/2\pi)$ is the reduced Planck's constant. With a unit cell volume of $a_0^3 = 5.75 \times 10^{-23}$ cm^{-3}, the expected saturation magnetization is ~185 emu/cm^3, as revealed by neutron diffraction [37]. The easy axis of Mn_4N thin films grown on cubic substrates lies along the [001] direction [25], [30]. The experimentally measured saturation magnetization of Mn_4N films grown on MgO and STO are ~145 emu/cm^3 at room temperature [25], comparable but smaller than the neutron diffraction result. It is much smaller when grown on GaN at only ~60 emu/cm^3 at room temperature [27], [36].

Fig. 2(a) shows the evolution of RHEED patterns during the deposition of Mn_4N layers at two growth temperatures. At a low growth temperature of $T_s = 150$ °C, the RHEED pattern starts as streaky and slightly diffuse in the initial nucleation stage. After the deposition of ~10 nm Mn_4N, the RHEED pattern evolves from streaks to diffraction spots, indicative of $Mn_4N(111)\|GaN(0001)$. Similar RHEED patterns have also been observed earlier for Mn_4N/SiC [27], [36] and other cubic materials such as MgO grown on hexagonal GaN [38]. This RHEED pattern persists until the end of the growth of the Mn_4N layer. The resulting film exhibits sixfold symmetry in the diffraction pattern as found by the rotational symmetry of the RHEED spots upon rotating the sample. This is expected, considering rotational twins [27], [36], [38]. Besides, barely visible weak ring-like features in RHEED at the end of growth hint that the film is starting to become polycrystalline.

The RHEED pattern and its evolution are drastically different when the growth temperature is raised to $T_s = 300$ °C, as seen in Fig. 2(a). At the initial nucleation stage, RHEED streaks along GaN [11$\bar{2}$0] direction become broad, and weak fractional peaks (indicated by arrows) appear. As the growth proceeds, the streaks become sharper and the RHEED pattern remains streaky till the end of growth, suggesting a 2-D growth mode with a smooth surface. When combined with the XRD results shown later, this RHEED pattern corresponds to the epitaxial relationship Mn_4N [1$\bar{1}$0]$\|$GaN [11$\bar{2}$0] and Mn_4N (001)$\|$GaN (0001). A similar epitaxial relationship was recently found in the Fe_4N/GaN system [39].

This epitaxial registry is different from the earlier report of Mn_4N/GaN using reactive MBE [36] and is somewhat

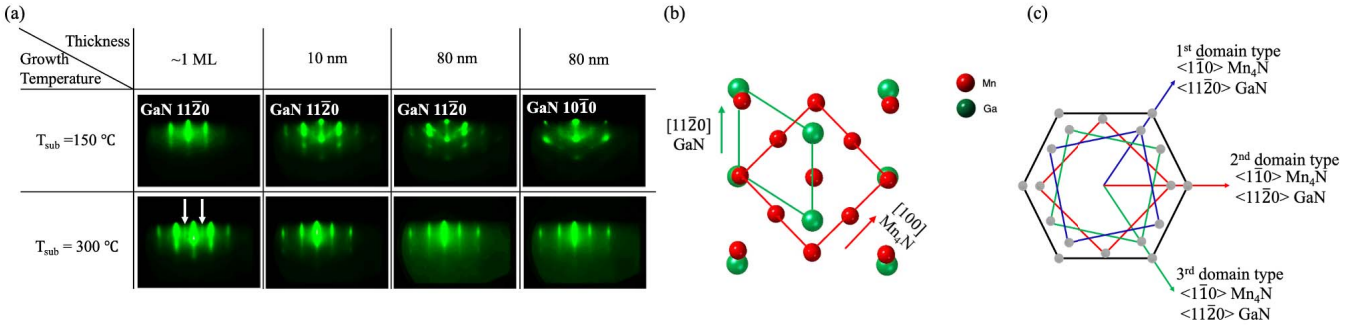

Fig. 2. (a) Evolution of the RHEED pattern during Mn_4N deposition for $T_s = 150$ °C and $T_s = 300$ °C (the white arrows indicate fractional peaks). (b) Schematic of epitaxial registry between GaN (0001) and Mn_4N (001) surfaces. (c) Schematic of the three equivalent domain variants of Mn_4N on GaN.

unexpected from the viewpoint of crystal symmetry. Because GaN is hexagonal, cubic Mn_4N is expected to grow with [111] orientation out-of-plane and exhibit a trigonal in-plane symmetry. RHEED patterns for Mn_4N layers grown at $T_s = 225$ °C and $T_s = 375$ °C (not shown) look similar to the $T_s = 300$ °C case. The RHEED pattern looks slightly diffusive by the end of the growth for $T_s = 375$ °C, possibly due to a rougher surface.

Fig. 2(b) shows a schematic of the potential epitaxial registry between GaN (0001) and Mn_4N (001) surfaces based on the RHEED of the Mn_4N/GaN sample grown at $T_s = 300$ °C. Nitrogen atoms are omitted for simplicity. This epitaxial relationship allows three equivalent in-plane stackings corresponding to three different methods for fitting a square in a hexagon, as shown in Fig. 2(c). This results in a total of 12-fold symmetry in the diffraction pattern of the Mn_4N film. Indeed, as shown in Fig. 2(a), the RHEED pattern looks identical along GaN [11$\bar{2}$0] and GaN [10$\bar{1}$0] azimuths by the end of the growth at $T_s = 300$ °C, consistent with 12-fold symmetry. Fig. 2(b) also shows that the lattice mismatch between Mn_4N and GaN is large (16%).

To further corroborate the epitaxial relationship between Mn_4N and GaN, symmetric $2\theta/\omega$ XRD scans of the films grown at various temperatures are compared in Fig. 3(a). At a low growth temperature of $T_s = 150$ °C, both Mn_4N (111) [indicated by the dashed line in Fig. 3(a)] and Mn_4N (002) XRD peaks are observed, along with peaks from the substrate, while no peaks corresponding to other phases are present. Therefore, the film deposited at $T_s = 150$ °C is polycrystalline Mn_4N, though nanoinclusions of other phase precipitates are not ruled out. Increasing the growth temperature to $T_s \geq 225$ °C suppresses the (111) oriented Mn_4N XRD peak, indicating that the films become almost c-axis aligned with no appreciable (111) orientation inclusion. It is worth noting that the Mn_4N crystal orientations in this study using plasma-assisted MBE are in sharp contrast to the earlier study [36] of Mn_4N on hexagonal SiC using reactive MBE, where only Mn_4N (111) XRD peak was reported.

Fig. 3(b) shows the X-ray ϕ-scan along [111] direction of the film grown at $T_s = 300$ °C. The peaks vividly show the 12-fold symmetry, further corroborating the proposed epitaxial registry shown in Fig. 2(c). The extracted c-axis lattice constants for Mn_4N grown on GaN are shown in Fig. 3(c) as a

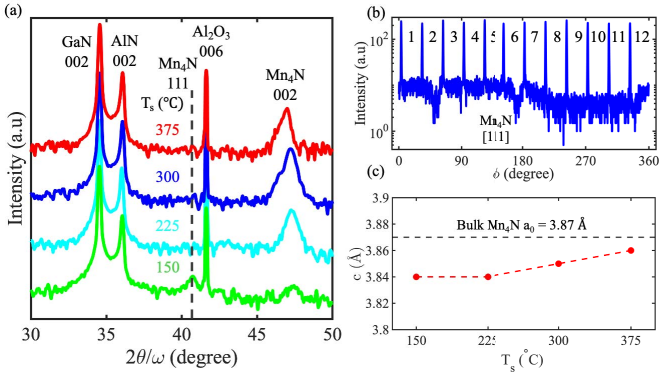

Fig. 3. (a) Symmetric $2\theta/\omega$ XRD scans for samples grown at different substrate temperatures (the dashed line indicates Mn_4N (111) peak). (b) ϕ scan along Mn_4N [111] for sample grown at $T_s = 300$ °C. (c) Evolution of out-of-plane lattice constants extracted from XRD scans (the dashed line indicates bulk lattice constant).

function of growth temperature. With the increase of growth temperature, the c-axis lattice constant gradually increases toward 3.87 Å, the bulk value [40], [41]. The evolution of the lattice constants of Mn_4N layers with growth temperature might be a reason for the sign-flip of the anomalous Hall resistance discussed later.

The 10×10 μm^2 AFM scans and corresponding rms roughness for Mn_4N films grown at different temperatures are shown in Fig. 4(a). The roughness is between 1 and 2 nm for growth temperatures $T_s \leq 300$ °C, and rougher at higher growth temperatures. Higher growth temperature also results in the presence of deep pits in the film. For example, pits with a depth larger than 15 nm measured by AFM are observed in Mn_4N film grown at $T_s > 300$ °C (not shown). For Mn_4N layers with smooth surfaces desired for magnetic tunnel junctions and spin–orbit torque devices, a low growth temperature is therefore needed in plasma-MBE. This is in contrast to the high ($T_s = 650$ °C) growth temperature found in the previous report by reactive MBE [36]. The low growth temperature is also attractive from a fabrication point-of-view whereby high-temperature degradation of other device components can be avoided. Fig. 4(b) shows a zoomed-in 2×2 μm^2 AFM scan for the Mn_4N film grown at $T_s = 300$ °C. Well-ordered cubic domains with three different

TABLE I

COMPARISON OF THE STRUCTURAL AND MAGNETIC PROPERTIES BETWEEN Mn_4N LAYERS GROWN ON MGO AND GAN AT VARIOUS SUBSTRATE TEMPERATURES (T_{SUB}: SUBSTRATE TEMPERATURE, t: FILM THICKNESS, RMS: ROOT MEAN SQUARE ROUGHNESS, c: OUT-OF-PLANE LATTICE CONSTANT, ρ_{xx}: LONGITUDINAL RESISTIVITY, ρ_{xy}: HALL RESISTIVITY, α_H: HALL ANGLE DEFINED AS (ρ_{xy}/ρ_{xx}), ZERO FIELD REMANENCE: $(\rho_{xy}(0))/(\rho_{xy}(1\ \mathrm{T}))$, H_c: COERCIVE FIELD AND M_s: SATURATION MAGNETIZATION). NOTE THAT ALL THE MAGNETIC PROPERTIES EXCEPT SATURATION MAGNETIZATION WERE EXTRACTED FROM ANOMALOUS HALL RESISTANCE HYSTERESIS LOOPS WITH MAGNETIC FIELD BETWEEN ±1 T.

Sample	Substrate	T_{sub} (°C)	t (nm)	RMS (nm)	c (Å)	In-plane symmetry	$\rho_{xx}{}^{300\ \mathrm{K}}$ ($\mu\Omega\cdot$cm)	$\rho_{xy}{}^{300\ \mathrm{K},\ 1\ \mathrm{T}}$ ($\mu\Omega\cdot$cm)	$\alpha_H{}^{300\ \mathrm{K},\ 1\mathrm{T}}$ (%)	Zero field Remanence	H_c (T)	M_s (emu/cc)
1	MgO	450	70	0.2	3.86	4-fold	170	1.92	1.13	0.97	0.30	130
2	GaN	150	80	1.0	3.84	6-fold	192	0.45	0.23	0.62	0.35	67
3	GaN	225	80	1.5	3.84	12-fold	174	1.02	0.59	0.75	0.45	95
4	GaN	300	80	1.6	3.85	12-fold	171	0.22	0.13	0.79	0.60	36
5	GaN	375	80	6.4	3.86	12-fold	164	0.26	0.16	0.90	0.70	58

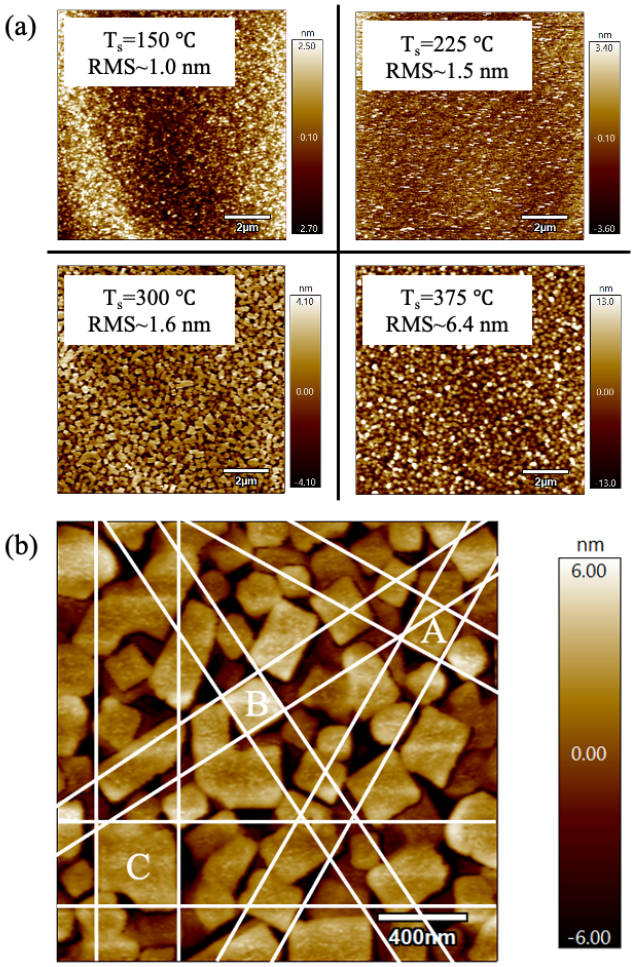

Fig. 4. (a) $10 \times 10\ \mu m^2$ AFM images and rms roughness for samples grown at different substrate temperatures. (b) $2 \times 2\ \mu m^2$ AFM image for sample grown at $T_s = 300$ °C (A, B, C and surrounding white lines mark domains with different orientations).

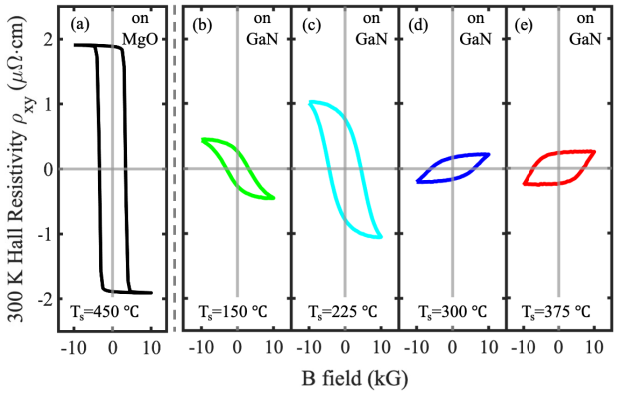

Fig. 5. Anomalous Hall resistance hysteresis loops between ±1 T magnetic field at 300 K for Mn_4N layers grown on MgO at (a) 450 °C and on GaN at (b) 150 °C, (c) 225 °C, (d) 300 °C, and (e) 375 °C. Note the flip in the loop orientation from (c) to (d), indicating n-type to p-type conversion.

orientations (marked as A, B, and C) are consistent with the aforementioned epitaxial relations and again highlight the 12-fold symmetry. Almost all domain edges are aligned along the 12-fold axes indicated by the overlaid lines.

Fig. 5 shows the room temperature Hall resistivity ρ_{xy} of Mn_4N layers grown on GaN at different temperatures, as well as a Mn_4N layer (~70 nm) grown on MgO at the optimal growth temperature of 450 °C for comparison. Clear hysteresis loops are observed in all the samples highlighting the magnetic behavior. It is worth pointing out that the 1 T magnetic field (the maximum magnetic field that can be applied by our measurement setup) might not be able to fully saturate the films. Magnetotransport measurements at higher magnetic fields are important future directions. Mn_4N films grown on GaN at low temperatures of $T_s \leq 225$ °C show n-type like anomalous Hall resistance, similar to the one grown on MgO seen in Fig. 5(a). The anomalous Hall resistance hysteresis loops of Mn_4N grown on GaN are not as square and exhibit larger coercivities compared to that on MgO. This is likely because of the larger density of crystal defects resulting from the lattice and symmetry mismatch between Mn_4N and GaN. Interestingly, for growth temperature above $T_s = 300$ °C, the Hall resistance of the Mn_4N films flips sign and shows p-type like behavior. Such room temperature p-type like anomalous Hall resistance has not been reported for Mn_4N on other substrates.

The longitudinal conductivities σ_{xx} of Mn_4N films on GaN in this study are around $6 \times 10^{-3}\ (\mu\Omega\cdot\mathrm{cm})^{-1}$, which fall in the dirty metal regime according to [42]. Consequently, the intrinsic contribution to the Hall conductivity due to the Berry

curvature (which depends sensitively on the bandstructure) likely dominates the anomalous Hall resistance in Mn_4N films on GaN. Since the lattice constants as shown in Fig. 3(c), and hence, the bandstructures of Mn_4N films vary with the growth temperature, the sign reversal of Hall resistance observed here is likely caused by the lattice distortions and consequent changes to the bandstructure and resulting Berry curvature. *Ab initio* bandstructure and Berry curvature calculations in the future can help unveil the origin of the observed sign reversal of the Hall resistance.

In Table I, we have summarized the structural, magneto-transport properties (extracted from anomalous Hall resistance hysteresis loops with a magnetic field between ± 1 T) and saturation magnetization of Mn_4N layers and their symmetry when grown on the control MgO substrate, and GaN at various substrate temperatures for easy comparison.

IV. Conclusion

Through the exploration of nucleation conditions and growth parameters, *c*-axis aligned Mn_4N thin films with smooth surfaces were grown on GaN substrates using plasma-assisted MBE in a previously unexplored growth window. Instead of growing with [111] orientation out-of-plane as expected from symmetry and a previous reactive MBE report, [001] orientation dominates the growth, especially at higher growth temperatures. Mn_4N layers grown on GaN exhibit 12-fold in-plane symmetry in the diffraction pattern due to the coexistence of three equivalent domain variants. The magnetic properties of Mn_4N grown on hexagonal GaN are comparable to those in earlier reports on cubic substrates such as MgO and can be tailored by varying the growth temperature. For example, with the increase of growth temperature, the anomalous Hall resistance hysteresis loop not only becomes squarer but also exhibits an interesting sign-flip from n-type to p-type between $T_s = 225$ °C and $T_s = 300$ °C. Such sign reversal has not been observed on other substrates and it is likely because of the evolution of lattice spacing, and hence, bandstructure with respect to growth temperature.

The strong tunability of the magnetic properties makes Mn_4N on GaN attractive for several applications. Particularly, Mn_4N grown at low temperatures of $T_s \leq 300$ °C have smooth surfaces, opening up the possibility for direct integration of spintronic devices such as magnetic tunnel junctions and spin–orbit torque devices with GaN-based electronic and photonic systems. Those grown at moderate temperatures of $T_s > 300$ °C have the preferable properties for applications where high perpendicular remanence are desired, such as magnetic recording and spin injection at remanence. These results reveal the significant potential of Mn_4N as an epitaxial ferrimagnet for new spintronic applications that take advantage of the wide bandgap semiconductor electronics and photonics platform. Microscopy analysis at Mn_4N/GaN interface is an ongoing research direction to better understand the unique epitaxial relationship between Mn_4N and GaN.

Acknowledgment

This work was supported in part by the Semiconductor Research Corporation (SRC) as nCORE under Grant 2758.001, in part by NSF through the Energy-Efficient Computing: from Devices to Architectures (E2CDA) Program under Grant ECCS 1740286 and Grant NewLAW EFRI 1741694, and in part by NSF through the Materials Research Science and Engineering Centers (MRSEC) Program under Grant DMR-1719875, the Cornell Center for Materials Research (CCMR), and Grant MRI DMR-1631282.

The authors would like to thank Prof. David Muller, Celesta Chang, Joseph Casamento, and Phillip Dang for helpful discussions.

References

[1] R. A. Ferreyra, C. Zhu, A. Teke, and H. Morkoç, "Group III nitrides," in *Springer Handbook of Electronic and Photonic Materials*. Cham, Switzerland: Springer, 2017, p. 1.

[2] D. Jena *et al.*, "The new nitrides: Layered, ferroelectric, magnetic, metallic and superconducting nitrides to boost the GaN photonics and electronics eco-system," *Jpn. J. Appl. Phys.*, vol. 58, no. SC, Jun. 2019, Art. no. SC0801.

[3] A. Banerjee, F. Doğan, J. Heo, A. Manchon, W. Guo, and P. Bhattacharya, "Spin relaxation in InGaN quantum disks in GaN nanowires," *Nano Lett.*, vol. 11, no. 12, pp. 5396–5400, Dec. 2011.

[4] J. H. Buß, J. Rudolph, F. Natali, F. Semond, and D. Hägele, "Anisotropic electron spin relaxation in bulk GaN," *Appl. Phys. Lett.*, vol. 95, no. 19, Nov. 2009, Art. no. 192107.

[5] S. Krishnamurthy, M. van Schilfgaarde, and N. Newman, "Spin lifetimes of electrons injected into GaAs and GaN," *Appl. Phys. Lett.*, vol. 83, no. 9, pp. 1761–1763, Sep. 2003.

[6] A. Song *et al.*, "Modulating room temperature spin injection into GaN towards the high-efficiency spin-light emitting diodes," *Appl. Phys. Exp.*, vol. 13, no. 4, Apr. 2020, Art. no. 043006.

[7] S. Jahangir, F. Doğan, H. Kum, A. Manchon, and P. Bhattacharya, "Spin diffusion in bulk GaN measured with MnAs spin injector," *Phys. Rev. B, Condens. Matter*, vol. 86, no. 3, Jul. 2012, Art. no. 035315.

[8] T.-E. Park *et al.*, "Large spin accumulation and crystallographic dependence of spin transport in single crystal gallium nitride nanowires," *Nature Commun.*, vol. 8, no. 1, pp. 1–7, Aug. 2017.

[9] A. Bhattacharya, M. Z. Baten, and P. Bhattacharya, "Electrical spin injection and detection of spin precession in room temperature bulk GaN lateral spin valves," *Appl. Phys. Lett.*, vol. 108, no. 4, Jan. 2016, Art. no. 042406.

[10] W. Stefanowicz *et al.*, "Experimental determination of Rashba spin-orbit coupling in wurtzite *n*-GaN: Si," *Phys. Rev. B, Condens. Matter*, vol. 89, no. 20, 2014, Art. no. 205201.

[11] R. Adhikari, M. Matzer, A. T. Martín-Luengo, M. C. Scharber, and A. Bonanni, "Rashba semiconductor as spin Hall material: Experimental demonstration of spin pumping in wurtzite n-GaN:Si," *Phys. Rev. B, Condens. Matter*, vol. 94, no. 8, Aug. 2016, Art. no. 085205.

[12] X. Luo *et al.*, "Spin–orbit torques in GaN/NiFe bilayers," *J. Phys. D, Appl. Phys.*, vol. 52, no. 1, Jan. 2019, Art. no. 015001.

[13] S. Hövel *et al.*, "Room temperature electrical spin injection in remanence," *Appl. Phys. Lett.*, vol. 93, no. 2, Jul. 2008, Art. no. 021117.

[14] D. Banerjee *et al.*, "Electrical spin injection using GaCrN in a GaN based spin light emitting diode," *Appl. Phys. Lett.*, vol. 103, no. 24, Dec. 2013, Art. no. 242408.

[15] M.-H. Ham, S. Yoon, Y. Park, L. Bian, M. Ramsteiner, and J.-M. Myoung, "Electrical spin injection from room-temperature ferromagnetic (Ga, Mn)N in nitride-based spin-polarized light-emitting diodes," *J. Phys., Condens. Matter*, vol. 18, no. 32, p. 7703, 2006.

[16] C. Zube *et al.*, "Spin injection in epitaxial MnGa(111)/GaN(0001) heterostructures," *J. Appl. Phys.*, vol. 123, no. 3, Jan. 2018, Art. no. 033906.

[17] E. Vetter *et al.*, "Observation of carrier concentration dependent spintronic terahertz emission from *n*-GaN/NiFe heterostructures," *Appl. Phys. Lett.*, vol. 117, no. 9, Aug. 2020, Art. no. 093502.

[18] Z. Zhang, H. Zhao, Y. Ren, B. Ma, and Q. Y. Jin, "Interface roughness effects on the performance of magnetic tunnel junctions," *Thin Solid Films*, vol. 515, nos. 7–8, pp. 3941–3945, Feb. 2007.

[19] Q. Shao *et al.*, "Role of dimensional crossover on spin-orbit torque efficiency in magnetic insulator thin films," *Nature Commun.*, vol. 9, no. 1, pp. 1–7, Dec. 2018.

[20] N. Chowdhury, Q. Xie, M. Yuan, K. Cheng, H. W. Then, and T. Palacios, "Regrowth-free GaN-based complementary logic on a Si substrate," *IEEE Electron Device Lett.*, vol. 41, no. 6, pp. 820–823, Jun. 2020.

[21] S. J. Bader *et al.*, "Gate-recessed E-mode p-channel HFET with high on-current based on GaN/AlN 2D hole gas," *IEEE Electron Device Lett.*, vol. 39, no. 12, pp. 1848–1851, Dec. 2018.

[22] T. Gushi *et al.*, "Large current driven domain wall mobility and gate tuning of coercivity in ferrimagnetic Mn_4N thin films," *Nano Lett.*, vol. 19, no. 12, pp. 8716–8723, 2019.

[23] M. Meng *et al.*, "Extrinsic anomalous Hall effect in epitaxial Mn_4N films," *Appl. Phys. Lett.*, vol. 106, no. 3, Art. no. 032407, 2015.

[24] M. Miao, A. Herwadkar, and W. R. Lambrecht, "Electronic structure and magnetic properties of Mn_3GaN precipitates in $Ga_{1-x}Mn_xN$," *Phys. Rev. B, Condens. Matter*, vol. 72, no. 3, 2005, Art. no. 033204.

[25] Y. Yasutomi, K. Ito, T. Sanai, K. Toko, and T. Suemasu, "Perpendicular magnetic anisotropy of Mn_4N films on MgO (001) and $SrTiO_3$ (001) substrates," *J. Appl. Phys.*, vol. 115, no. 17, 2014, Art. no. 17A935.

[26] T. Hirose, T. Komori, T. Gushi, K. Toko, and T. Suemasu, "Perpendicular magnetic anisotropy in ferrimagnetic Mn_4N films grown on $(LaAlO_3)_{0.3}(Sr_2TaAlO_6)_{0.7}$ (001) substrates by molecular beam epitaxy," *J. Cryst. Growth*, vol. 535, Apr. 2020, Art. no. 125566.

[27] Z. Zhang *et al.*, "Magnetic properties of MBE grown Mn_4N on MgO, SiC, GaN and Al_2O_3 substrates," *AIP Adv.*, vol. 10, no. 1, Jan. 2020, Art. no. 015238.

[28] T. Gushi *et al.*, "Millimeter-sized magnetic domains in perpendicularly magnetized ferrimagnetic Mn_4N thin films grown on $SrTiO_3$," *Jpn. J. Appl. Phys.*, vol. 57, no. 12, Dec. 2018, Art. no. 120310.

[29] X. Shen, A. Chikamatsu, K. Shigematsu, Y. Hirose, T. Fukumura, and T. Hasegawa, "Metallic transport and large anomalous Hall effect at room temperature in ferrimagnetic Mn_4N epitaxial thin film," *Appl. Phys. Lett.*, vol. 105, no. 7, Aug. 2014, Art. no. 072410.

[30] S. Isogami, K. Masuda, and Y. Miura, "Contributions of magnetic structure and nitrogen to perpendicular magnetocrystalline anisotropy in antiperovskite ε-Mn_4N," *Phys. Rev. Mater.*, vol. 4, no. 1, Jan. 2020, Art. no. 014406.

[31] K. Kabara and M. Tsunoda, "Perpendicular magnetic anisotropy of Mn_4N films fabricated by reactive sputtering method," *J. Appl. Phys.*, vol. 117, no. 17, May 2015, Art. no. 17B512.

[32] K. Ito *et al.*, "Manipulation of saturation magnetization and perpendicular magnetic anisotropy in epitaxial $Co_xMn_{4-x}N$ films with ferrimagnetic compensation," *Phys. Rev. B, Condens. Matter*, vol. 101, no. 10, Mar. 2020, Art. no. 104401.

[33] H. Mitarai *et al.*, "Magnetic compensation at two different composition ratios in rare-earth-free $Mn_{4-x}Co_xN$ ferrimagnetic films," *Phys. Rev. Mater.*, vol. 4, no. 9, Sep. 2020, Art. no. 094401.

[34] T. Komori *et al.*, "Magnetic and magneto-transport properties of Mn_4N thin films by Ni substitution and their possibility of magnetic compensation," *J. Appl. Phys.*, vol. 125, no. 21, Jun. 2019, Art. no. 213902.

[35] S. Ghosh *et al.*, "Current-driven domain wall dynamics in ferrimagnetic nickel-doped Mn_4N films: Very large domain wall velocities and reversal of motion direction across the magnetic compensation point," *Nano Lett.*, vol. 21, no. 6, pp. 2580–2587, Mar. 2021.

[36] S. Dhar, O. Brandt, and K. H. Ploog, "Ferrimagnetic Mn_4N(111) layers grown on 6H-SiC(0001) and GaN(0001) by reactive molecular-beam epitaxy," *Appl. Phys. Lett.*, vol. 86, no. 11, Mar. 2005, Art. no. 112504.

[37] W. Takei, R. Heikes, and G. Shirane, "Magnetic structure of Mn_4N-type compounds," *Phys. Rev.*, vol. 125, no. 6, p. 1893, 1962.

[38] H. S. Craft, J. F. Ihlefeld, M. D. Losego, R. Collazo, Z. Sitar, and J.-P. Maria, "MgO epitaxy on GaN (0002) surfaces by molecular beam epitaxy," *Appl. Phys. Lett.*, vol. 88, no. 21, May 2006, Art. no. 212906.

[39] M. Kimura and S. Hasegawa, "Growth evolution of γ-Fe_4N films on GaN(0001) and their interfacial structure," *Jpn. J. Appl. Phys.*, vol. 55, no. 5S, May 2016, Art. no. 05FD02.

[40] H. Yang, H. Al-Brithen, E. Trifan, D. C. Ingram, and A. R. Smith, "Crystalline phase and orientation control of manganese nitride grown on MgO(001) by molecular beam epitaxy," *J. Appl. Phys.*, vol. 91, no. 3, pp. 1053–1059, Feb. 2002.

[41] K. Ito *et al.*, "Perpendicular magnetic anisotropy in $Co_xMn_{4-x}N$ (x = 0 and 0.2) epitaxial films and possibility of tetragonal Mn_4N phase," *AIP Adv.*, vol. 6, no. 5, May 2016, Art. no. 056201.

[42] S. Onoda, N. Sugimoto, and N. Nagaosa, "Intrinsic versus extrinsic anomalous Hall effect in ferromagnets," *Phys. Rev. Lett.*, vol. 97, no. 12, Sep. 2006, Art. no. 126602.